# High-resolution *ex vivo* nanoCT reveals 3D architecture of the adult male mouse lower urogenital tract

Ajinkya R. Limkar[1,2,3], Simran M. Sharma[3], William A. Ricke[3,4]*

1 Medical Scientist Training Program, University of Wisconsin-Madison School of Medicine and Publish Health, Madison, Wisconsin, United States of America, 2 Molecular and Cellular Pharmacology Graduate Program, University of Wisconsin-Madison School of Medicine and Public Health, Madison, Wisconsin, United States of America, 3 Department of Urology, University of Wisconsin-Madison, Madison, Wisconsin, United States of America, 4 George M. O'Brien Urology Research Center of Excellence, University of Wisconsin-Madison, Madison, Wisconsin, United States of America

* rickew@urology.wisc.edu

## Abstract

Benign prostatic hyperplasia (BPH) is the most common cause of lower urinary tract symptoms/dysfunction (LUTS/LUTD) in aging men. Over the past 30 years, the prevalence of BPH has increased by 122%, rising from 50.7 million cases in 1990 to 112.5 million in 2021. It is expected that this number will continue to rise over the next 15 years with the global aging population. Although mouse models are invaluable for studying human disease, gross anatomical differences between human and murine prostates complicate their translational relevance for BPH/LUTS research. The purpose of this study was to develop and validate a nanoCT-based imaging approach to enable detailed anatomical analysis of the murine lower urinary tract, with the dual goals of advancing tools for LUTD research and improving the translational relevance of mouse models to human prostate disease. Advancements in nano-computed tomography (nanoCT) have enabled high-resolution characterization of murine organ anatomy, providing new insights into how morphological differences contribute to pathology. To accomplish this, whole lower urogenital tracts from 8-week-old healthy male C57BL/6J mice and microdissected prostatic urethras were imaged on a v|tome|x M or nanotom M nano-CT system, respectively. Images were processed for 2D segmentation and subsequent 3D reconstruction. Our approach enabled high-resolution visualization and characterization of the murine lower urogenital tract, including the urinary bladder, prostate lobes, seminal vesicles, and ductus deferens, as well as the microscopic ductal architecture of the prostatic urethra. The resulting 3D reconstructions preserved native anatomical relationships and allowed for comparisons between murine and human prostate anatomy; however, our findings are limited in that nanoCT is inherently an *ex vivo* analysis and only healthy, young C57BL/6J mice were used and pathology was not assessed in the current study.

Together, these findings establish a method that can be used for assessing anatomical and morphological changes associated with LUTD development, while also highlighting key anatomical similarities that enhance the translational relevance of mouse models for human prostate disease.

## Introduction

Benign prostatic hyperplasia (BPH) arises from a loss of tissue homeostasis within the aging prostate and is the most prevalent cause of lower urinary tract dysfunction (LUTD) in older men [1]. Over the past three decades, the global burden of BPH has risen significantly, with number of prevalent cases rising from 50.7 million in 1990 to 112.5 million in 2021, an increase of 122% [2]. This trend is expected to continue alongside demographic shifts, as it is estimated that by 2050, approximately 22% of the world's population will be over 60 years of age [3]. BPH often presents clinically as lower urinary tract symptoms (LUTS), including urinary frequency, urgency, and nocturia, which have significant impacts on quality of life and total healthcare expenditures [4–6]. It is estimated that upward of 90% of all men over the age of 80 experience some degree of prostate mediated LUTS [7]. Analysis of years lived with disability (YLD) of common urological conditions from 1990–2017 found that BPH accounts for approximately 2.4 million YLD, three times greater than that of prostate cancer [8]. As the global population continues to age, conditions like BPH/LUTS will become more clinically significant, highlighting the need for more scientific investigation. Mouse models have become indispensable for the study of human disease. In context of LUTD, sex-steroids, inflammation, mechanical insult, and natural aging have all been used to study disease development and progression in mice [9–12]. The human prostate is a single, encapsulated organ surrounded by a thick fibromuscular capsule, whereas the murine prostate comprises multiple lobes that sit freely within the peritoneal cavity [13–15]. These fundamental differences in the gross anatomy of the human and murine prostates have raised concerns about the suitability of the mouse as a model for studying prostate associated pathology.

The development of small animal, high-resolution imaging technologies have significantly advanced our understanding of anatomical similarities and differences between humans and animal models such as the mouse. Techniques such as micro-computer tomograph (microCT) and magnetic resonance imaging (MRI) have been widely applied to image and reconstruct complex organs such as the murine liver, kidney, and lung. This has led to innovations in the development of therapeutics and the study of how morphological changes in pathology lead to functional decline [16–18]. Although fundamental to our understanding of the anatomical-pathological relationship, techniques like microCT and MRI are often limited by the maximum achievable spatial resolution. Alternative approaches that provide higher-resolution visualization frequently rely on 3D reconstruction of H&E-stained serial tissue sections, a process that is both time intensive and laborious [19,20]. Nano-computed tomography (nanoCT) expands the capabilities of microCT by achieving spatial

resolution down to approximately 200 nm, contrasted to the 6–12 µm range typical of microCT and the approximate 100 µm resolution limit of MRI for soft tissue visualization. NanoCT has been used to 3D reconstruct fine anatomical structures like individual pulmonary acini, cerebral vasculature, and lacunae voids within cortical bone [21–23].

In the context of the murine lower urogenital tract, we have previously developed an MRI based method that has been used to image and reconstruct various organs including the urinary bladder, prostate lobes, and urethra. Furthermore, we have shown that this method can be used to characterize changes in urogenital tract anatomy associated with the development of LUTD [11,24,25]. Although faster than reconstruction of serial sections, our MRI-based method lacked the spatial resolution to appreciate the finer anatomical details such as prostatic duct counts and branching patterns. Despite these advancements, our understanding of how the unique anatomy of the mouse lower urogenital tract correlates with the human prostate remains incomplete. Here, we aim to increase our understanding of murine lower urogenital tract morphology and ultimately bridge the anatomical gap between model systems.

In this report, we describe a novel nanoCT-based approach that allows for higher-resolution visualization and reconstruction of the murine lower urogenital tract. By resolving fine anatomical structures in three dimensions, this method enables a more comprehensive assessment of murine prostate organization and its spatial relationships to the urethra and surrounding tissues. Importantly, this approach allows for precise, quantitative measurements of the urethral lumen, rhabdosphincter, and periurethral region that are directly relevant to the study of lower urinary tract dysfunction. These insights provide an important step toward improving anatomical comparisons between mouse and human prostates, ultimately enhancing the translational relevance of murine models for investigating BPH/LUTS.

## Methods and materials

### Animals

All animal experiments were conducted under the protocols approved by the University of Wisconsin Animal Care and Use Committee (Protocol Number: M005570). All authors comply with the ARRIVE guidelines, and all methods were performed in accordance with the relevant guidelines and regulations. Male C57BL/6J mice (cat# 000664) were obtained from the Jackson Laboratory (Bar Harbor, ME). Animals were housed under standard laboratory conditions with a 12:12 light/dark cycle and provided with food and water *ad libitum*. Within 7 days of receipt, naïve, untreated mice were euthanized with carbon dioxide asphyxiation followed by cardiac puncture. Anesthesia, analgesics, and efforts to alleviate suffering were not needed in the experimental design.

### Preparation of tissues and contrast stains

Five urogenital tracts (UGTs) were dissected from untreated, healthy 8-week-old C57BL/6J mice as previously described [12]. Whole UGTs included the bladder, seminal vesicles, prostate lobes, and urethra, with the distal ductus deferens, ureters, testes, and gonadal fat removed. Additionally, four UGTs from untreated, healthy 8-week-old C57BL/6J mice were microdissected to isolate the urethra by removing the bladder, seminal vesicles, and prostate lobes [12]. Tissues were fixed in 10% neutral buffered formalin and stored in 70% ethanol until further processing. For soft tissue contrast, specimens were stained in Lugol's iodine (10% diluted iodine-potassium iodide solution; Sigma-Aldrich, St. Louis, MO) for 24 hours at room temperature [26]. To minimize evaporation and motion artifacts during imaging, samples were embedded in 2% low-melting point agarose/PBS gel within 30 × 24 × 5 mm disposable plastic fixtures (Fisher Tissue Path, Fisher Scientific, Hampton, NH).

### NanoCT imaging protocol

Five whole murine urogenital tracts and four microdissected murine urethra specimens were immobilized inside plastic fixtures and scanned using nanoCT systems. Whole UGTs were imaged using a v|tome|x M nanoCT system (phoenix x-ray,

Waygate Technologies USA, LP; Skaneateles, New York) at 100 kV and 100 µA with a 1.0 mm copper filter, an 11.39 µm voxel size, and a 500.1 ms exposure time. Three frames were averaged, and one was skipped per rotation as the sample stage rotated 360° to collect 2,220 images per scan. Microdissected urethra specimens were scanned using a nanotom M nanoCT system (phoenix x-ray, Waygate Technologies USA) at 65 kV and 250 µA with a diamond-coated tungsten target, a 0.254 mm aluminum filter, a spot size of 0, a 3.5 µm voxel size, and a 500 ms exposure time. Three frames were averaged, and one was skipped per rotation, with 2,000 images collected per scan. Image acquisition and reconstruction of raw data were performed using Datos|x 2 software (v2.8.2 for whole UGTs; v2.6.1 for urethra specimens). Comprehensive nanoCT scanning parameters can be found in S1 Table.

### 3D reconstruction and measurements of selected anatomic measurements

NanoCT tomographs containing axial, coronal, and sagittal data from each scanned tissue (whole urogenital tract and microdissected urethra) were imported into DragonFly 3D World (Comet Tech, Herrengasse, Switzerland) for 3D reconstruction. Anatomical structures were identified and manually segmented using voxel thresholding based on the Otsu Method. Representative 2D tomographs and 3D reconstructions are shown of a single whole urogenital tract and single microdissected prostatic urethra.

Anatomical measurements including urethral luminal area, diameter, perimeter, rhabdosphincter thickness, and prostatic duct count were taken at a standardized point within the prostatic urethra. This reference point was determined by identifying the axial slice where the rhabdosphincter fully encircled the prostatic urethra, then selecting a location 50 µm caudal to it. Urethral luminal area and perimeter were calculated using the polygon ROI tool, while luminal diameter was measured as the horizontal distance across the lumen. Rhabdosphincter thickness was determined by averaging eight measurements across its internal and external boundaries. Prostatic ducts were defined as well demarcated, luminal epithelial structures surrounding the urethral lumen and were counted manually in a single axial slice at the standardized reference point. Prostatic urethra length was measured in the coronal view as the distance from the start of the rhabdosphincter to the apex of the verumontanum.

### Assessment of inter-rater reliability

To assess inter-rater agreement for segmentation and quantitative analysis data between independent raters, inter-class correlation coefficient (ICC) was calculated for each quantitative variable. Three raters were trained in 2D segmentation and 3D reconstruction of microdissected urethral tissue specimens. ICC values were calculated using a two-way, mixed-effects model for single measurements and absolute agreement using the *irr* package in R Studio (v. 2025.05.1 + 513). Raters quantified urethral luminal area, diameter, and perimeter, rhabdosphincter thickness, prostatic duct count, and prostatic urethra length. ICC values were interpreted based on established agreement thresholds of: < 0.5 = poor, 0.5–0.75 = moderate, 0.75–0.9 = good, and >0.9 = excellent reliability [27]. To evaluate segmentation overlap between raters, Dice coefficients (DC) were calculated from 3D binary masks exported as TIFF stacks from Dragonfly 3D World. Segmentations from two independent raters were loaded and binarized using Python 3.12 (Spyder IDE, Anaconda) and the scikit-image (v0.25.0) and NumPy libraries as previously described [28]. A Dice coefficient equal to 1.0 represents perfect overlap between each rater's segmentation.

## Results

Macroscopically, the murine male lower urogenital tract consists of the urinary bladder, paired seminal vesicles, urethra, and paired anterior, ventral, dorsal, and lateral prostate lobes (Fig 1). The dorsal and lateral lobes are often collectively referred to as the dorsolateral prostate.

The structural organization of the murine lower urogenital tract is illustrated by representative coronal and axial nanoCT images (Fig 2). Whole-organ scans at 11.39 µm/voxel (Figs 2A and 2B) show the relative positioning of the bladder, seminal
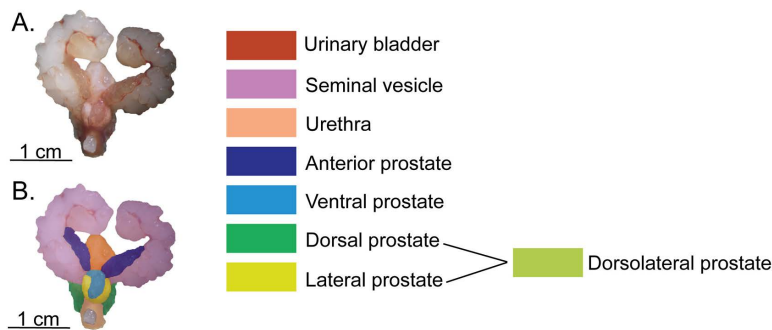
**Fig 1. Illustration and color segmentation of the healthy 8-week-old C57BL/6J male murine lower urogenital tract.** A) *Ex vivo* image of the lower urogenital tract. B) Color-coded segmentation highlighting key structures, including the seminal vesicles, urinary bladder, prostate lobes, and urethra. The color scheme will be used in all subsequent Figs.

https://doi.org/10.1371/journal.pone.0326004.g001

vesicles, and prostate lobes. Manual segmentation (Figs 2C and 2D) delineates each structure segmented in the 2D plane, facilitating both quantitative and morphological analyses. Higher-resolution imaging at 3.5 µm/voxel (Fig 2E) captures fine anatomical details within the prostatic urethra, including the rhabdosphincter and periurethral prostatic ducts, with corresponding manual 2D segmentations (Fig 2F). Lugol's iodine staining provided enhanced soft tissue contrast, allowing differentiation between glandular, muscular, and connective tissues. 2D segmentation enabled precise 3D reconstruction of each structure (Fig 2G). Together, these data establish a comprehensive anatomical framework for subsequent qualitative and quantitative analyses of individual structures in the healthy adult murine lower urogenital tract, which are detailed in the following sections.

## NanoCT of the whole lower urogenital tract

NanoCT imaging at the 11.39 µm/voxel spatial resolution provided detailed visualization of the healthy 8-week-old C57Bl/6J male murine lower urogenital tract, capturing both its gross anatomical organization and fine structural features. At this lower resolution, even finer anatomy such epithelial folding patterns, large ductal architecture, and tissue boundaries were able to be visualized.

## Urinary bladder and urethral lumen

NanoCT imaging provides high-resolution visualization of the urinary bladder, enabling assessment of features relevant to lower urinary tract dysfunction (Fig 3A). Lugol's iodine contrast effectively delineates the detrusor muscle from surrounding connective tissue and the urothelium, allowing for detailed evaluation of bladder wall architecture. Two-dimensional images reveal urothelial invaginations and areas of variable wall thickness. In the case of lower urinary tract dysfunction, acute or chronic urinary retention often results in overdistension of the urinary bladder and can lead to detrusor muscle atrophy and flattening of bladder rugae, both of which may be identified on nanoCT imaging.

## Seminal vesicles

NanoCT imaging enables detailed visualization of the paired seminal vesicles, revealing their complex internal architecture and luminal folds (Fig 3B). The protein-rich seminal fluid provides strong contrast enhancement with Lugol's iodine.

## Ductus deferens

NanoCT imaging shows the ductus deferens as paired muscular tubes with concentric hyperdense smooth muscle layers surrounding a narrow lumen (Fig 3C). The paired structures function to support sperm transport from the epididymis to the verumontanum. The distal ampullary glands appear as hyperdense alveolar structures at the base of the ductus deferens.
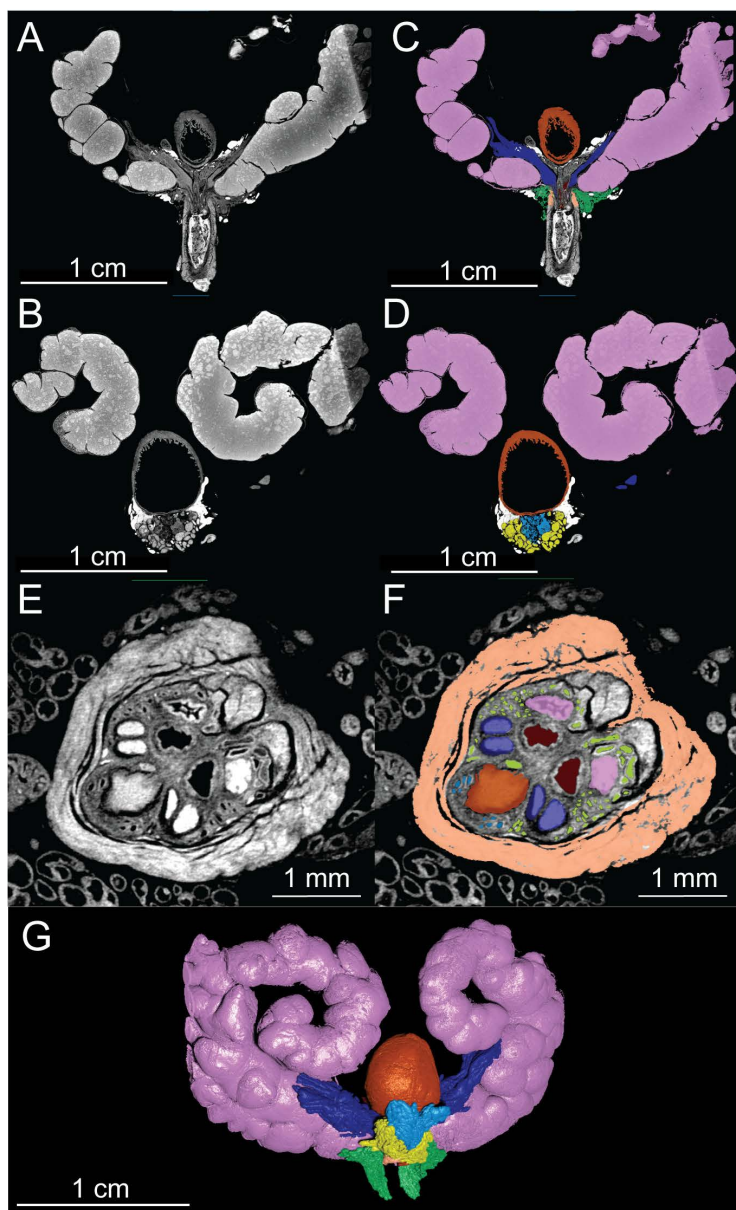
**Fig 2. NanoCT tomographs and 2D segmentation of a healthy 8-week-old C57BL/6J male murine lower urogenital tract.** A-B) Coronal nanoCT views of the intact murine urogenital tract (11.39 μm/voxel). C-D) Manual segmentation of key anatomical structures. E) High-resolution axial nanoCT image of the murine prostatic urethra (3.5 μm/voxel). F) Corresponding manual segmentation highlighting relevant structures within the prostatic urethra. G) 3D reconstruction of the intact urogenital tract. Urinary bladder (orange), seminal vesicle (pink), rhabdosphincter (light orange), anterior prostate (dark blue), ventral prostate (light blue), lateral prostate (yellow), dorsal prostate (green).

https://doi.org/10.1371/journal.pone.0326004.g002

## Rhabdosphincter

The rhabdosphincter, or external urethral sphincter, is clearly visualized on contrast-enhanced nanoCT due to high Lugol's iodine uptake within the circumferential striated skeletal muscle fibers (Fig 3D). Emerging caudal to the bladder neck and encasing the prostatic urethra, nanoCT may be used to assess sphincter integrity, thickness, and structure which may have implications for urinary continence.
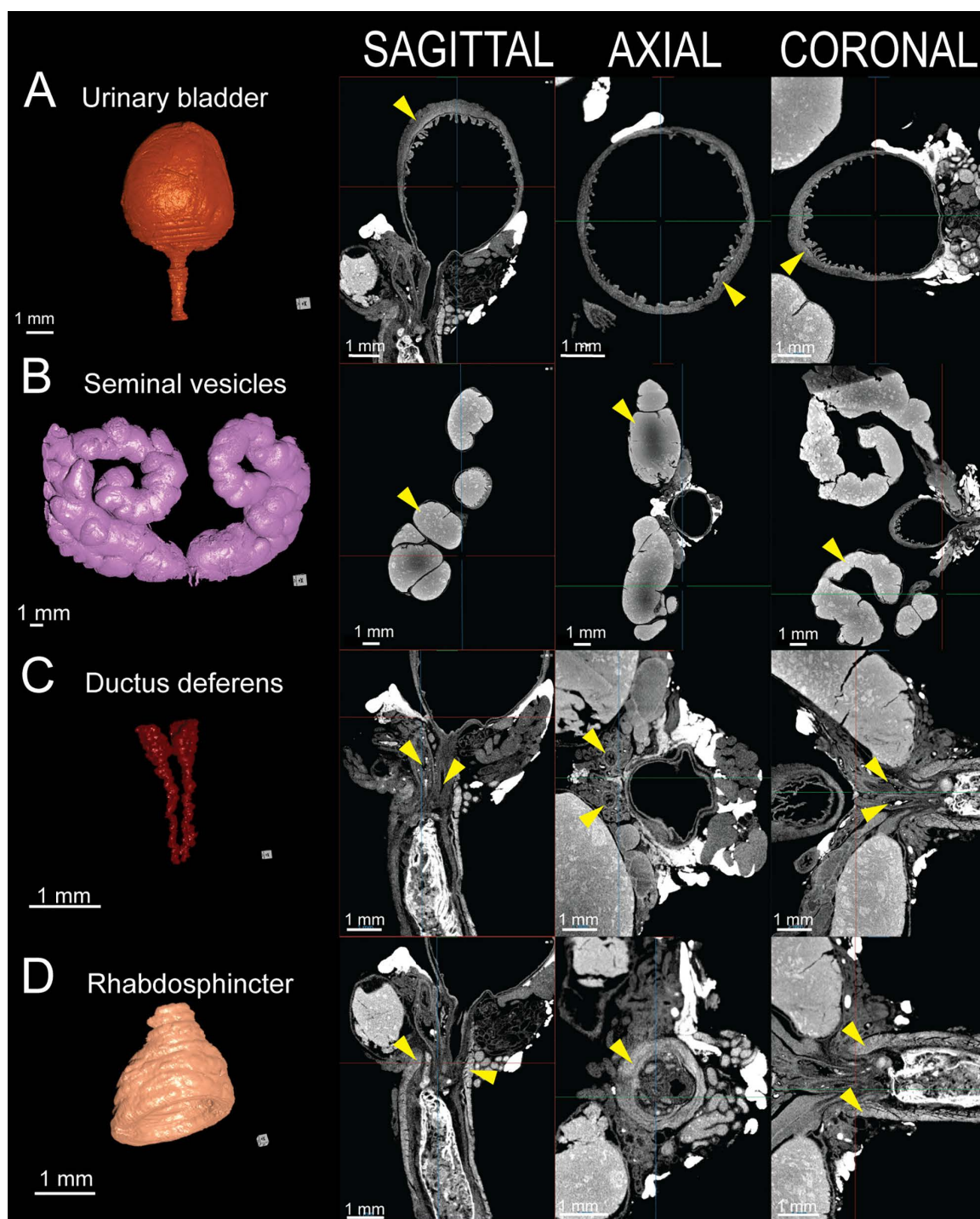
**Fig 3. 3D reconstruction and 2D tomographic views of key structures in the healthy 8-week-old C57BL/6J male murine lower urogenital tract.**
A) Urinary bladder. B) Seminal vesicles. C) Ductus deferens. D) Rhabdosphincter. Next to each 3D reconstruction, corresponding sagittal (left), axial (center), and coronal (right) nanoCT slices illustrate the anatomical organization. Urinary bladder (orange), seminal vesicle (pink), ductus deferens (red), rhabdosphincter (light orange).

https://doi.org/10.1371/journal.pone.0326004.g003

## Prostate lobes

The murine prostate consists of four paired lobes anterior, ventral, dorsal, and lateral. Each are distinguishable on nanoCT imaging by their unique ductal morphology and contrast enhancement patterns. Lugol's iodine staining highlights both glandular and stromal components. The anterior prostate displays uniformly hyperdense regions, attributed to abundant prostatic secretions and dense stromal smooth muscle, both of which enhance iodine uptake (Fig 4A). In contrast, the ventral prostate features hypodense ducts with large lumens and minimal intraglandular folding, reflecting sparse secretions and reduced stromal density (Fig 4B). The dorsal prostate is visualized as small, hypodense acinar clusters extending caudal the prostatic urethra into the membranous urethra and dorsally surrounding the inferior aspects of the seminal vesicles (Fig 4C). Finally, the lateral prostate, positioned between the ventral and dorsal lobes, comprises intermediate-sized ducts with moderate luminal folding and high contrast uptake (Fig 4D).

## NanoCT of the prostatic urethra

NanoCT imaging at the 3.5 µm/voxel spatial resolution provided visualization of the finer structures in the healthy 8-week-old C57Bl/6J male murine prostatic urethra region. At this high spatial resolution, microscopic ductal architecture of the urethral lumen, seminal vesicle, ductus deferens, and prostate lobes as well as their branching patterns were able to be segmented, reconstructed, and observed (Fig 5A). In the region of the prostatic urethra, the urethral lumen begins as a narrow, elliptical structure just caudal to the bladder neck, gradually expanding distally as it receives secretions from the prostate and merges with the prostatic ducts (Fig 5B). NanoCT imaging revealed that the seminal vesicles contribute two ducts to the prostatic urethra (Fig 5C). Similarly, the paired ductus deferens contribute two ducts to the prostatic urethra (Fig 5D). These paired ducts maintain their spatial orientation along the length of the urethra, merging cranially to the verumontanum. Unlike in humans, where the seminal vesicle and vas deferens unite to form the ejaculatory ducts within the prostate, murine ducts remain distinct until they converge at the verumontanum. High-resolution nanoCT imaging was able to visualize the individual ducts originating from the different prostate lobes. The anterior prostate lobe contributes two large, paired ducts (Fig 5E), which traverse medially from their lateral origins to merge with the superior aspect of the urethral lumen. These ducts do not undergo major branching as they extend cranially to caudally. In contrast, the ventral prostate lobe gives rise to 3–5 smaller ducts that enter the prostatic urethra (Fig 5F). These ducts, also oriented along the cranial-caudal axis, originate from the inferior-most aspect of the prostatic urethra, exhibiting some minor branching before merging with the urethral lumen. The dorsal and lateral prostate lobes contribute numerous ducts that enter the prostatic urethra (Fig 5G). These ducts are difficult to trace back to their lobe of origin due to extensive branching and tortuosity. As such, the ducts from both lobes are collectively referred to as the dorsolateral prostate ducts. These ducts exhibit complex expansion and distribution patterns before joining the urethral lumen at various levels.

The shape and structure of the prostatic urethra varies significantly along its length, influenced by the periurethral ductal system at each point. High-resolution nanoCT imaging allowed for visualization of this internal structure. 2D tomographs revealed that the rhabdosphincter begins approximately 200–300 µm distal to the bladder neck at the ventral aspect of the urethra (Fig 6B). From this point, the muscle extends obliquely from ventral to dorsal, fully encircling the prostatic urethra (Fig 6D). Notably, this region (approximately 500–700 µm in length) marks the entry point for all primary ducts into the prostatic urethra: the urethral lumen (from the bladder), paired seminal vesicles, paired ductus deferens, and ducts from each prostate lobe. The point at which the rhabdosphincter fully encircled the prostatic urethra was the used here to define the anatomical start of the prostatic urethra region. Axial scans showed evidence of convergence of the paired anterior and ventral prostate ducts with the urethral lumen as early as 100–150 µm caudal to this landmark (Fig 6E and Fig 6F). To ensure consistency in our quantitative analyses, all measurements were performed 50 µm caudal to the point of rhabdosphincter closure. This location was selected to establish a reproducible anatomical landmark that captures the onset of the prostatic urethra while minimizing variability associated with more distal regions where the risk of omitting anatomical structures is higher.
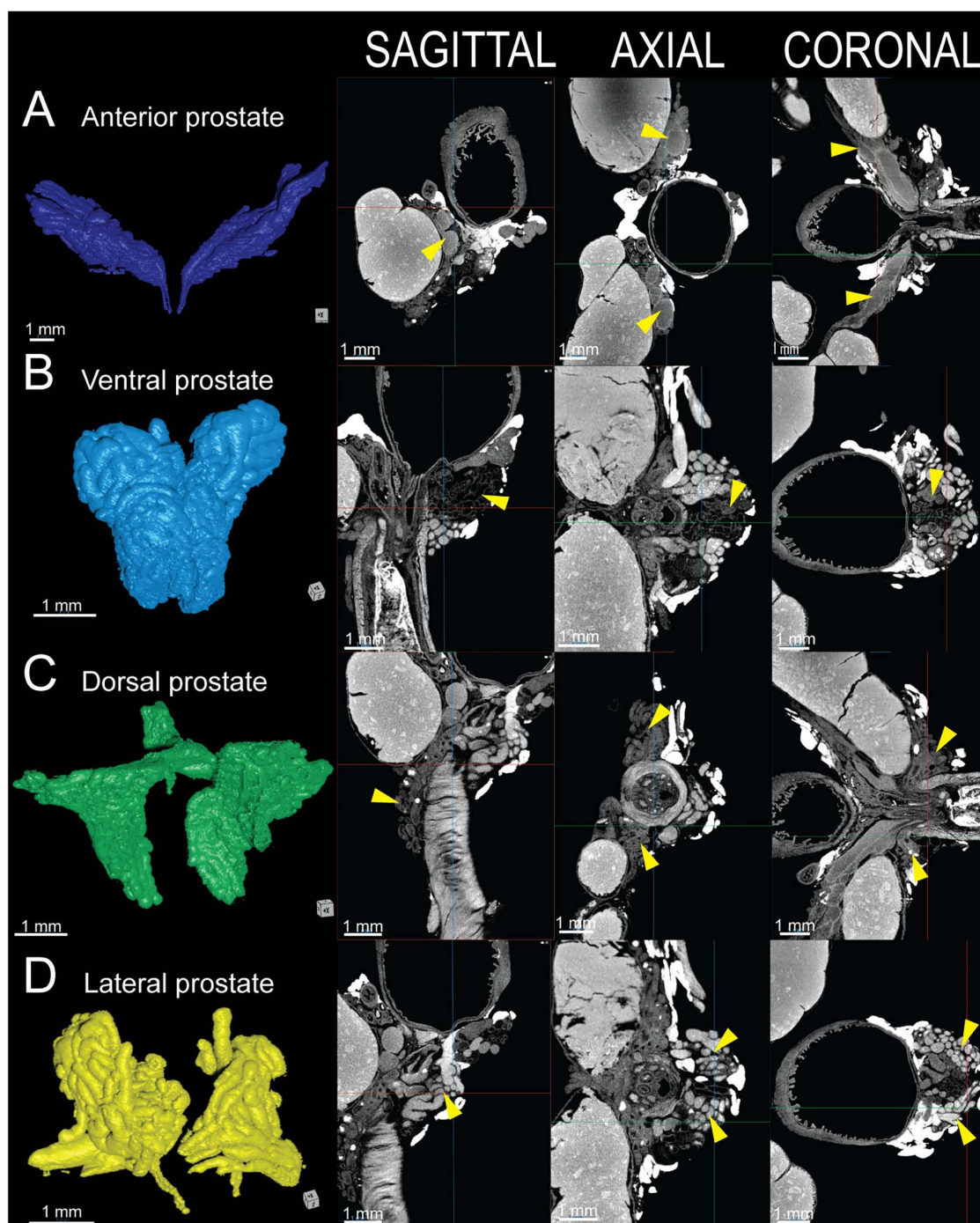
**Fig 4. 3D reconstruction and 2D tomographic views of the healthy 8-week-old C57BL/6J male murine prostate lobes.** A) Anterior prostate (dark blue). B) Ventral prostate (light blue). C) Dorsal prostate (green). D) Lateral prostate (yellow). Next to each 3D reconstruction, corresponding sagittal (left), axial (center), and coronal (right) nanoCT slices depict the anatomical organization.
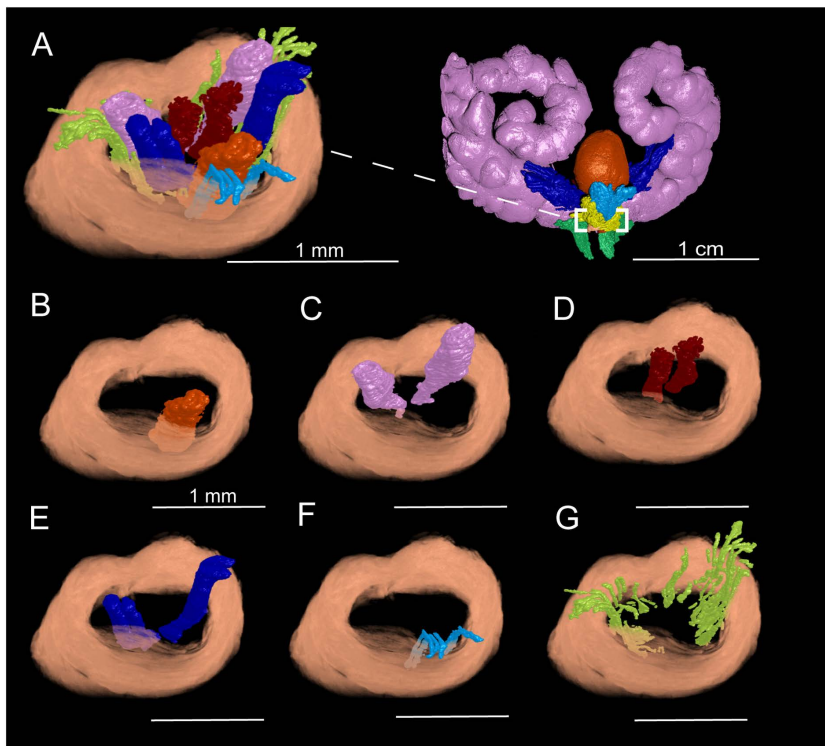
**Fig 5. 3D reconstruction of the healthy 8-week-old C57BL/6J male murine prostatic urethra.** A) Isolated prostatic urethra (dashed box). B) Urethral lumen (orange). C) Seminal vesicle ducts (pink) D) Ductus deferens (red). E) Anterior prostate ducts (dark blue). F) Ventral prostate ducts (light blue). G) Dorsolateral prostate ducts (lime green).

## Quantitative analysis of key features of the prostatic urethra

Contrast-enhanced nanoCT imaging of the murine prostatic urethra enabled for detailed measurements of key structural features *ex vivo* without the need for histologic sectioning. These key measurements are of particular interest in the study of lower urinary tract dysfunction. In this study, urethral lumen area, diameter, and perimeter, rhabdosphincter thickness, prostatic duct count, and prostatic urethral length were reported. A summary of prostatic urethra measurements are shown in Table 1. Urethral lumen area ranged from $0.07\,mm^2$ to $0.16\,mm^2$. Luminal diameter ranged from $0.21\,mm$ to $0.39\,mm$. Luminal perimeter ranged from $0.79\,mm$ to $1.44\,mm$. Rhabdosphincter thickness ranged from $0.1887$ to $0.2375\,mm$. Prostatic duct number ranged from 28 to 47 ducts. Finally, prostatic urethra length ranged from $1.09\,mm$ to $1.69\,mm$.

## Discussion

In this study, we provide a comprehensive, high-resolution 3D anatomical characterization of the murine male lower urogenital tract using nanoCT imaging. By preserving the spatial organization of key structures, particularly the prostatic urethra and associated prostate lobes, we present an anatomical framework that offers new insights into the mouse model's relevance for studying human prostate biology and pathology, including lower urinary tract dysfunction (LUTD) and benign prostatic hyperplasia (BPH). This detailed anatomical mapping provides a foundation for more refined investigations into the role of prostatic architecture and metrics in disease development.

Our findings corroborate existing knowledge of the murine lower urogenital tract structure while adding a level of 3D detail that was previously unattainable with traditional methods such as histology [29]. NanoCT imaging enhanced
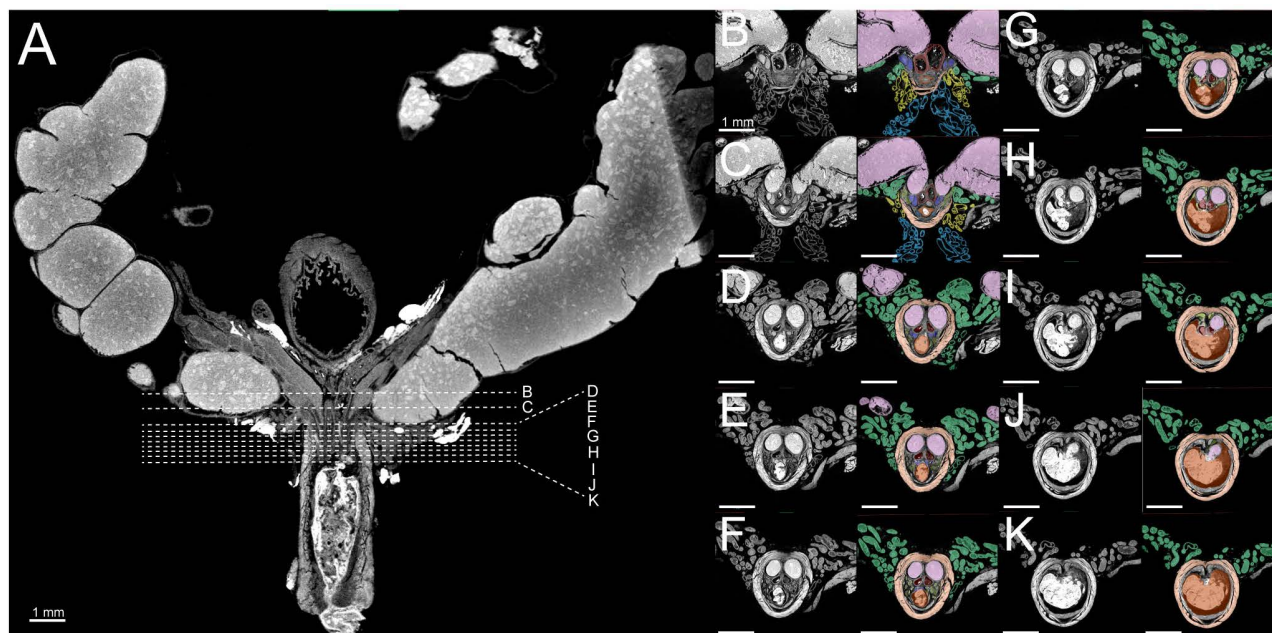
**Fig 6. Axial Images of the of the healthy 8-week-old C57BL/6J male murine prostatic urethra.** A) Coronal reference image indicating the approximate locations of axial slices. B-K) Serial axial nanoCT images of the prostatic urethra and surrounding structures along the cranial-caudal axis. Sections begin caudal to the bladder neck and extend to the verumontanum. Urethral lumen (orange), seminal vesicle (pink), rhabdosphincter (light orange), anterior prostate (dark blue), ventral prostate (light blue), lateral prostate (yellow), dorsal prostate (green), dorsolateral prostate ducts (lime green).

https://doi.org/10.1371/journal.pone.0326004.g006

**Table 1. Quantitative analysis of key features of the mouse prostatic urethra.**

| Urethral Lumen | | | | | |
|---|---|---|---|---|---|
| Mouse | Area (mm²) | Diameter (mm) | Perimeter (mm) | Rhabdosphincter thickness (mm) | Prostatic duct count | Prostatic urethra length (mm) |
| 1 | 0.16 | 0.39 | 1.44 | 0.1887 | 32 | 1.69 |
| 2 | 0.07 | 0.35 | 0.99 | 0.2375 | 28 | 1.13 |
| 3 | 0.03 | 0.21 | 0.79 | 0.1925 | 31 | 1.49 |
| 4 | 0.09 | 0.36 | 1.16 | 0.2375 | 47 | 1.09 |
| Mean ± SD | 0.0875 ± 0.054 | 0.33 ± 0.080 | 1.095 ± 0.275 | 0.2140 ± 0.027 | 34.5 ± 8.504 | 1.35 ± 0.289 |

Values represent quantitative measurements of anatomical features in the mouse prostatic urethra. Measurements include urethral lumen area, diameter, and perimeter; rhabdosphincter thickness; prostatic duct count; and prostatic urethra length. Data are presented for individual specimens (n = 4) and as mean ± standard deviation.

https://doi.org/10.1371/journal.pone.0326004.t001

visualization of the urinary bladder, seminal vesicles, ductus deferens, and prostate lobes, with a particular focus on the prostatic urethra. The ability to visualize ductal structures and their precise relationships to the urethral lumen is key to understanding pathologies like prostatic hyperplasia and LUTD. Unlike traditional high-resolution tissue reconstruction methods, which require embedding, sectioning, H&E staining, imaging, and slide by slide segmentation and reconstruction, nanoCT allowed us to reconstruct our tissues while maintaining native anatomical architecture in a significantly shorter time [19,20].

In both mice and humans, the periurethral zone posits itself an area of significant homology. In the human prostate, the transition zone, which encircles the proximal urethra and accounts for 5–10% of total prostate volume, is the primary site of BPH-related pathology [30,31]. Anatomically, the human prostate transition zone consists of two regions whose ducts emerge from the posterolateral urethral wall, just proximal to the urethral orifice and the preprostatic sphincter, a collection of smooth muscle surrounding the proximal urethra [32–34]. These ducts extend laterally, curve anteriorly, and branch toward the bladder neck, with medial ducts penetrating the sphincter. Our nanoCT reconstructions reveal that the murine prostatic urethra is surrounded by a dense network of ducts, primarily arising from the dorsal and lateral prostate lobes and to a lesser extent the anterior and ventral prostate. These ducts exhibit significant branching and direct connections to the urethral lumen, paralleling the human transition zone's ductal architecture. Furthermore, like the fibromuscular capsule encasing the human prostate, the murine periurethral region is enclosed by thick circumferential muscle fibers comprising the rhabdosphincter. As periurethral ducts in the mouse prostatic urethra expand in size or number, due to aging or hormonal related changes, the rhabdosphincter may act as a mechanical barrier, restricting outward growth and directing expansion into the urethral lumen, thereby impinging on the urethral space [11,12]. This mirrors the glandular and stromal hyperplasia in BPH that expands upon the urethral lumen, contributing to obstruction and LUTS [32]. These shared anatomical features, particularly ductal architecture, proximity to the urethral lumen, and periurethral organization, support the conclusion that the murine prostatic urethra closely parallels the human transition zone and should serve as the primary focus for studies of prostate-mediated lower urinary tract dysfunction in murine models. Our data further revealed that the anterior and ventral prostate lobes exhibit comparatively less communication with the urethral lumen and simpler ductal branching patterns. These lobes are anatomically positioned more distally from the urethral lumen, suggesting that they may play a less prominent role in modeling periurethral disease processes.

The ability for quantitative analysis of the prostatic urethra further strengthens the utility of nanoCT in future anatomical and pathological studies. We have previously shown that an MRI-based methodology can be used to quantify pathological changes within the murine lower urogenital tract [11,24,25]. However, this was limited to a resolution of $100 \times 100 \times 100$ $\mu m^3$, whereas our improved method achieves a spatial resolution of $3.5 \times 3.5 \times 3.5$ $\mu m^3$. Our data provides valuable baseline measurements of key structural features, including urethral lumen area, rhabdosphincter thickness, duct number, and prostatic urethra length. These measurements can serve as critical metrics for evaluating disease progression and the effects of therapeutic interventions in future studies of BPH and LUTD. As our methodology is dependent on manual segmentation, we acknowledge the presence of inherent observer bias. To address this, we assessed inter-rater reliability using both interclass correlation coefficients (ICC) and Dice coefficients (DC). ICC was calculated for each quantitative parameter from three independent raters (S2 Table). Most variables demonstrate excellent reliability (ICC > 0.9), including urethral lumen area (ICC = 0.990), perimeter (ICC = 0.989) and prostatic urethra length (ICC = 0.942). Moderate to good reliability was observed for prostatic urethra duct count (ICC = 0.676) and rhabdosphincter thickness (ICC = 0.610) which may reflect an inherent variability in anatomical boundary identification for these features. To further evaluate segmentation overlap, 3D binary masks from two independent raters were compared using the Dice coefficients (S3 Table). Structures such as the urethral lumen (DC = 0.9523), ductus deferens (DC = 0.9806), rhabdosphincter (DC = 0.9626), and anterior prostate ducts (DC = 0.9558) showed highest overlap. Lower agreement was evident with smaller structures such as the ventral (DC = 0.8820) and dorsolateral prostate ducts (DC = 0.7945) which likely reflect the anatomical complexity and branching nature of these structures. Previous studies in the mouse have shown that an increase in prostatic duct number within the periurethral region is associated with lower urinary tract dysfunction [11,12]. Therefore, duct count and branching morphogenesis can be studied in greater detail in the context of aging or treatment with antiproliferative agents (e.g., 5-α reductase inhibitors) and may lead to insights into how changes in in these structures contribute to urinary function.

In this study, we aimed to provide a high-resolution anatomical framework for studying the murine lower urogenital tract. The detailed 3D reconstructions and quantitative measurements presented here offer improved methods for exploring structural changes associated with BPH and LUTD in murine models. NanoCT is particularly valuable because it preserves native

tissue architecture while providing higher spatial resolution than microCT or MRI, making it suitable for detailed anatomical imaging. However, several limitations remain. NanoCT is inherently an *ex vivo* imaging modality, which restricts its ability to assess longitudinal anatomical changes over the course of disease progression. In contrast, other imaging technologies like MRI, ultrasound, and optical methods enable *in vivo* imaging and can be used to monitor structural and functional changes in living animals over time [35]. For example, MRI offers adequate soft tissue contrast though it is limited by longer acquisition and image processing times. Ultrasound provides real-time visualization of superficial structures with reasonable spatial resolution but is limited by its inability to penetrate bone or air-filled tissues. Optical modalities such as bioluminescence and fluorescence imaging allow for high-throughput, transgene-based tracking of cell function or viability, though their utility is limited by low anatomical resolution and requires genetic manipulation of the animal model [36]. Moreover, while contrast enhancement is necessary for nanoCT imaging, it carries the potential to introduce artifacts or alter tissue integrity, although the use of Lugol's iodine as an *ex vivo* contrast agent has not been shown to compromise downstream standard histological and immunohistochemical analyses [37,38]. Finally, this study uses tissues from healthy, 8-week-old male C57BL/6J mice and does not consider anatomical variability due to age, sex, mouse strain, or pathology. Future studies will address these limitations and leverage this anatomical framework to investigate how such variables influence the murine lower urogenital tract. More specifically, we plan to use this method which offers a baseline for future pathologic studies, to evaluate the effects of age on murine lower urinary tract anatomy, validate mouse models of BPH/LUTD such as the hormone-induced model, and assess the translatability of mouse models in BPH research by investigate the effects of clinically relevant BPH therapies (5-α reductase inhibitors and α-blockers) on periurethral anatomy. Overall, despite its limitations, nanoCT remains a powerful tool for high-resolution, high-throughput anatomical analysis relevant to prostate biology and disease research.

## Supporting information

**S1 Table. NanoCT scanning parameters.** NanoCT acquisition parameters used for imaging whole mouse urogenital tracts and microdissected urethra specimens. Scans were performed using either the v|tome|x M or nanotom M systems. Key parameters include voltage, current, filter material, voxel size, exposure settings, and total number of projection images collected per 360° rotation.
(DOCX)

**S2 Table. Interclass Correlation Coefficient (ICC) to assess inter-rater reliability.** Interclass Correlation Coefficients (ICC) with corresponding p-values assessing inter-rater reliability for quantitative measurements of the mouse prostatic urethra. ICC values were calculated from three independent raters. Interpretation thresholds are as follows: < 0.5 = poor, 0.5–0.75 = moderate, 0.75–0.9 = good, and >0.9 = excellent reliability.
(DOCX)

**S3 Table. Dice Coefficients (DC) to assess segmentation inter-rater variability.** Dice Coefficients (DC) quantifying inter-rater segmentation variability for selected anatomical structures within the mouse lower urogenital tract. The DC measures spatial overlap between segmentations performed by independent raters, where 0 indicates no overlap and 1 indicates perfect overlap.
(DOCX)

## Author contributions

**Conceptualization:** Ajinkya Ravindra Limkar, William A Ricke.

**Data curation:** Ajinkya Ravindra Limkar.

**Formal analysis:** Ajinkya Ravindra Limkar.

**Funding acquisition:** Ajinkya Ravindra Limkar, William A Ricke.

**Investigation:** Ajinkya Ravindra Limkar, Simran Miraya Sharma.

**Methodology:** Ajinkya Ravindra Limkar.

**Project administration:** Ajinkya Ravindra Limkar.

**Supervision:** William A Ricke.

**Writing – original draft:** Ajinkya Ravindra Limkar.

**Writing – review & editing:** Ajinkya Ravindra Limkar, Simran Miraya Sharma, William A Ricke.

## References

1. Abdelmoteleb H, Jefferies ER, Drake MJ. Assessment and management of male lower urinary tract symptoms (LUTS). Int J Surg. 2016;25:164–71. https://doi.org/10.1016/j.ijsu.2015.11.043 PMID: 26654899

2. Chen X, Yang S, He Z, Chen Z, Tang X, Lin Y, et al. Comprehensive analysis of the global, regional, and national burden of benign prostatic hyperplasia from 1990 to 2021. Sci Rep. 2025;15(1):5644. https://doi.org/10.1038/s41598-025-90229-3 PMID: 39955408

3. Newgard CB, Sharpless NE. Coming of age: molecular drivers of aging and therapeutic opportunities. J Clin Invest. 2013;123(3):946–50. https://doi.org/10.1172/JCI68833 PMID: 23454756

4. Creta M, Russo GI, Bhojani N, Drake MJ, Gratzke C, Peyronnet B, et al. Bladder outlet obstruction relief and symptom improvement following medical and surgical therapies for lower urinary tract symptoms suggestive of benign prostatic hyperplasia: a systematic review. Eur Urol. 2024;86(4):315–26. https://doi.org/10.1016/j.eururo.2024.04.031 PMID: 38749852

5. Park S, Ryu J m, Lee M. Quality of life in older adults with benign prostatic hyperplasia. Healthcare. 2020;8(2).

6. Speakman M, Kirby R, Doyle S, Ioannou C. Burden of male lower urinary tract symptoms (LUTS) suggestive of benign prostatic hyperplasia (BPH) - focus on the UK. BJU Int. 2015;115(4):508–19. https://doi.org/10.1111/bju.12745 PMID: 24656222

7. Barry MJ, Fowler FJ, Bin L, Oesterling JE. A nationwide survey of practicing urologists: current management of benign prostatic hyperplasia and clinically localized prostate cancer. J Urol. 1997;158(2):488–91.

8. Launer BM, McVary KT, Ricke WA, Lloyd GL. The rising worldwide impact of benign prostatic hyperplasia. BJU Int. 2021;127(6):722–8. https://doi.org/10.1111/bju.15286 PMID: 33124118

9. Austin JC, Chacko SK, DiSanto M, Canning DA, Zderic SA. A male murine model of partial bladder outlet obstruction reveals changes in detrusor morphology, contractility and Myosin isoform expression. J Urol. 2004;172(4 Pt 1):1524–8. https://doi.org/10.1097/01.ju.0000138045.61378.96 PMID: 15371884

10. Funahashi Y, O'Malley KJ, Kawamorita N, Tyagi P, DeFranco DB, Takahashi R, et al. Upregulation of androgen-responsive genes and transforming growth factor-β1 cascade genes in a rat model of non-bacterial prostatic inflammation. Prostate. 2014;74(4):337–45. https://doi.org/10.1002/pros.22668 PMID: 24446128

11. Liu TT, Thomas S, Mclean DT, Roldan-Alzate A, Hernando D, Ricke EA, et al. Prostate enlargement and altered urinary function are part of the aging process. Aging (Albany NY). 2019;11(9):2653–69. https://doi.org/10.18632/aging.101938 PMID: 31085797

12. Nicholson TM, Ricke EA, Marker PC, Miano JM, Mayer RD, Timms BG, et al. Testosterone and 17β-estradiol induce glandular prostatic growth, bladder outlet obstruction, and voiding dysfunction in male mice. Endocrinology. 2012;153(11):5556–65. https://doi.org/10.1210/en.2012-1522 PMID: 22948219

13. Cunha GR, Vezina CM, Isaacson D, Ricke WA, Timms BG, Cao M, et al. Development of the human prostate. Differentiation. 2018;103:24–45. https://doi.org/10.1016/j.diff.2018.08.005 PMID: 30224091

14. Ittmann M. Anatomy and histology of the human and murine prostate. Cold Spring Harb Perspect Med. 2018;8(5):a030346. https://doi.org/10.1101/cshperspect.a030346 PMID: 29038334

15. Treuting PM, Dintzis SM, Frevert CW, Liggitt D, Montine KS. Comparative anatomy and histology: a mouse and human atlas. 1st ed. London: Elsevier; 2012.

16. Ehling J, Bábíčková J, Gremse F, Klinkhammer BM, Baetke S, Knuechel R, et al. Quantitative micro-computed tomography imaging of vascular dysfunction in progressive kidney diseases. J Am Soc Nephrol. 2016;27(2):520–32. https://doi.org/10.1681/ASN.2015020204 PMID: 26195818

17. Fiebig T, Boll H, Figueiredo G, Kerl HU, Nittka S, Groden C, et al. Three-dimensional in vivo imaging of the murine liver: a micro-computed tomography-based anatomical study. PLoS One. 2012;7(2):e31179. https://doi.org/10.1371/journal.pone.0031179 PMID: 22363574

18. Shofer S, Badea C, Auerbach S, Schwartz DA, Johnson GA. A micro-computed tomography-based method for the measurement of pulmonary compliance in healthy and bleomycin-exposed mice. Exp Lung Res. 2007;33(3–4):169–83. https://doi.org/10.1080/01902140701364458 PMID: 17558678

19. Kiemen AL, Braxton AM, Grahn MP, Han KS, Babu JM, Reichel R. CODA: quantitative 3D reconstruction of large tissues at cellular resolution. Nature Methods. 2022;19(11):1490–9.

20. Uchtmann KS, Taylor JA, Timms BG, Stahlhut RW, Ricke EA, Ellersieck MR, et al. Fetal bisphenol A and ethinylestradiol exposure alters male rat urogenital tract morphology at birth: Confirmation of prior low-dose findings in CLARITY-BPA. Reprod Toxicol. 2020;91:131–41. https://doi.org/10.1016/j.reprotox.2019.11.007 PMID: 31756437

21. Duvall CL, Taylor WR, Weiss D, Guldberg RE. Quantitative microcomputed tomography analysis of collateral vessel development after ischemic injury. Am J Physiol Heart Circ Physiol. 2004;287(1):H302-10. https://doi.org/10.1152/ajpheart.00928.2003 PMID: 15016633

22. Khoury BM, Bigelow EMR, Smith LM, Schlecht SH, Scheller EL, Andarawis-Puri N, et al. The use of nano-computed tomography to enhance musculoskeletal research. Connect Tissue Res. 2015;56(2):106–19. https://doi.org/10.3109/03008207.2015.1005211 PMID: 25646568

23. McDonough JE, Yuan R, Suzuki M, Seyednejad N, Elliott WM, Sanchez PG, et al. Small-airway obstruction and emphysema in chronic obstructive pulmonary disease. N Engl J Med. 2011;365(17):1567–75. https://doi.org/10.1056/NEJMoa1106955 PMID: 22029978

24. McLean DT, Rutkowski DR, Liu T, Hernando D, Ricke WA, Roldán-Alzate A. MRI-based method for lower urinary tract dysfunction in adult male mice. Am J Clin Exp Urol. 2019;7(3):153–8. PMID: 31317054

25. Nguyen JL, Ricke EA, Liu TT, Gerona R, MacGillivray L, Wang Z, et al. Bisphenol-A analogs induce lower urinary tract dysfunction in male mice. Biochem Pharmacol. 2022;197:114889. https://doi.org/10.1016/j.bcp.2021.114889 PMID: 34979091

26. Gignac PM, Kley NJ. Iodine-enhanced micro-CT imaging: methodological refinements for the study of the soft-tissue anatomy of post-embryonic vertebrates. J Exp Zool B Mol Dev Evol. 2014;322(3):166–76. https://doi.org/10.1002/jez.b.22561 PMID: 24482316

27. Koo TK, Li MY. A guideline of selecting and reporting intraclass correlation coefficients for reliability research. J Chiropr Med. 2016;15(2):155–63. https://doi.org/10.1016/j.jcm.2016.02.012 PMID: 27330520

28. Anderson BM, Wahid KA, Brock KK. Simple python module for conversions between DICOM images and radiation therapy structures, masks, and prediction arrays. Pract Radiat Oncol. 2021;11(3):226–9. https://doi.org/10.1016/j.prro.2021.02.003 PMID: 33607331

29. Oliveira DSM, Dzinic S, Bonfil AI, Saliganan AD, Sheng S, Bonfil RD. The mouse prostate: a basic anatomical and histological guideline. Bosn J Basic Med Sci. 2016;16(1):8–13. https://doi.org/10.17305/bjbms.2016.917 PMID: 26773172

30. Kaplan SA, Te AE, Pressler LB, Olsson CA. Transition zone index as a method of assessing benign prostatic hyperplasia: correlation with symptoms, urine flow and detrusor pressure. J Urol. 1995;154(5):1764–9. https://doi.org/10.1016/s0022-5347(01)66779-x PMID: 7563342

31. Zlotta AR, Djavan B, Damoun M, Roumeguere T, Petein M, Entezari K, et al. The importance of measuring the prostatic transition zone: an anatomical and radiological study. BJU Int. 1999;84(6):661–6. https://doi.org/10.1046/j.1464-410x.1999.00214.x PMID: 10510112

32. McNeal JE. Normal histology of the prostate. Am J Surg Pathol. 1988;12(8):619–33. https://doi.org/10.1097/00000478-198808000-00003 PMID: 2456702

33. Oelrich TM. The urethral sphincter muscle in the male. Am J Anat. 1980;158(2):229–46. https://doi.org/10.1002/aja.1001580211 PMID: 7416058

34. Yucel S, Baskin LS. An anatomical description of the male and female urethral sphincter complex. J Urol. 2004;171(5):1890–7. https://doi.org/10.1097/01.ju.0000124106.16505.df PMID: 15076301

35. de Kemp RA, Epstein FH, Catana C, Tsui BMW, Ritman EL. Small-animal molecular imaging methods. J Nucl Med. 2010;51 Suppl 1(0 1):18S-32S. https://doi.org/10.2967/jnumed.109.068148 PMID: 20457793

36. Lyons SK. Advances in imaging mouse tumour models in vivo. J Pathol. 2005;205(2):194–205. https://doi.org/10.1002/path.1697 PMID: 15641018

37. Apps JR, Hutchinson JC, Arthurs OJ, Virasami A, Joshi A, Zeller-Plumhoff B, et al. Imaging invasion: Micro-CT imaging of adamantinomatous craniopharyngioma highlights cell type specific spatial relationships of tissue invasion. Acta Neuropathol Commun. 2016;4(1):57. https://doi.org/10.1186/s40478-016-0321-8 PMID: 27260197

38. Xia C-W, Gan R-L, Pan J-R, Hu S-Q, Zhou Q-Z, Chen S, et al. Lugol's iodine-enhanced Micro-CT: a potential 3-D imaging method for detecting tongue squamous cell carcinoma specimens in surgery. Front Oncol. 2020;10:550171. https://doi.org/10.3389/fonc.2020.550171 PMID: 33194607